JOURNAL OF GEOPHYSICAL RESEARCH, VOL. 102, NO. D14, PAGES 16,861–16,870, JULY 27, 1997

# Sensitivity of multiangle remote sensing observations to aerosol sphericity

Ralph Kahn, Robert West, Duncan McDonald, and Brian Rheingans
Jet Propulsion Laboratory, California Institute of Technology, Pasadena

Michael I. Mishchenko
NASA Goddard Institute for Space Studies, New York

**Abstract.** Multiangle, multispectral remote sensing observations, such as those anticipated from the Earth Observing System (EOS) multiangle imaging spectroradiometer (MISR), can distinguish spherical from nonspherical particles over calm ocean for mineral-dust-like particles with the range of sizes and column amounts expected under natural conditions. The ability to make such distinctions is critical if remote sensing of atmospheric aerosol properties is to provide significant new contributions to our understanding of the global-scale, clear-sky solar radiation balance. According to theoretical simulations the measurements can retrieve column optical depth for nonspherical particles to an accuracy of at least 0.05 or 10%, whichever is larger. In addition, three to four distinct size groups between 0.1 and 2.0 microns effective radius can be identified at most latitudes.

## 1. Introduction

In a recent paper, *Mishchenko et al.* [1995] studied the implications of assuming spherical particles in the retrieval of aerosol properties from remote sensing data, when nonspherical particles are present in the atmosphere. They demonstrate that for observations of dust-like aerosols over ocean, if a retrieval of total column optical depth is performed based on an assumption of spherical particles when in fact the particles are nonspherical, the results can be seriously in error. For the cases studied, the systematic error in total column optical depth is very sensitive to the geometry of the observation and can be arbitrarily large when simulated monospectral satellite measurements at a single emission angle are used in the retrieval, even assuming noiseless data.

The systematic errors demonstrated by *Mishchenko et al.* [1995] are unacceptably large for climate change studies. The magnitude of direct radiative effects from atmospheric aerosols is as yet uncertain, but it may be comparable to the size of the anticipated incremental greenhouse warming due to a doubling of atmospheric $CO_2$ [*Andreae*, 1995; *Penner et al.*, 1994; *Kiehl and Briegleb*, 1993; *Charlson et al.*, 1992; *Hansen and Lacis*, 1990]. Dust-like particles, which are likely to be nonspherical, make important contributions to the optical depth over large regions of the planet [*Tegen and Fung*, 1994].

Currently, satellite-based remote sensing instruments provide our best hope of obtaining the spatial and temporal coverage required for global monitoring of atmospheric aerosols. Although the only global-scale satellite-based retrieval of total column aerosol optical depth now in routine operation relies on a single channel of AVHRR data [*Rao et al.*, 1989; R. B. Husar et al., Satellite sensing of tropospheric aerosols over the oceans with NOAA/AVHRR, submitted to *Journal of Geophysical Research*, 1996], new satellite remote sensing instruments with multiangle and multispectral capabilities are being built. We present in this paper a theoretical study of the ability of multiangle and multispectral remote sensing techniques to distinguish between spherical and nonspherical particles. This study is part of our program to characterize the performance of the multiangle imaging spectroradiometer (MISR) instrument, which is scheduled for launch into polar orbit on the EOS-AM1 platform in June 1998 [*Diner et al.*, 1991].

The MISR instrument will measure the upwelling visible radiance from Earth in four spectral bands centered at 443, 555, 670, and 865 nm, at each of nine emission angles spread out in the forward and aft directions along the flight path at ±70.5°, ±60.0°, ±45.6°, ±26.1°, and nadir. The spatial sampling rate is 275 m the cross-track direction at all angles. Over a period of 7 min a 360-km-wide swath of Earth comes into the view of the cameras at each of the nine emission angles, providing a wide range of scattering angle coverage for each surface location. The data will be used to characterize aerosol optical depth, aerosol type, surface albedo and bidirectional reflectance, and cloud properties. Global coverage will be acquired about once in 9 days at the equator; the nominal mission lifetime is 6 years.

## 2. Modeling the Observations

For this study, we use single-scattering phase functions and albedos for spherical and nonspherical particles similar to those generated by *Mishchenko et al.* [1995, 1996]. The nonspherical particles are modeled as a mixture of polydisperse prolate and oblate spheroids with a uniform distribution of aspect ratios ranging between 1.4 and 2.2. (To accurately model the optical properties of naturally occurring nonspherical particles, the critical condition is to have a spectrum of aspect ratios as broad as this [*Mishchenko et al.*, 1996; *West et al.*, this issue].) Both spherical and nonspherical particle sizes are given by power law distributions, with $n(r) = C$ for $r \le r_1$, $n(r) = C(r_1/r)^3$ for $r_1 \le r < r_2$, and $n(r) = 0$ for $r \ge r_2$. Here $r$ is the particle radius for spherical particles and the radius of



Paper number 96JD01934.
0148-0227/97/96JD-01934$09.00

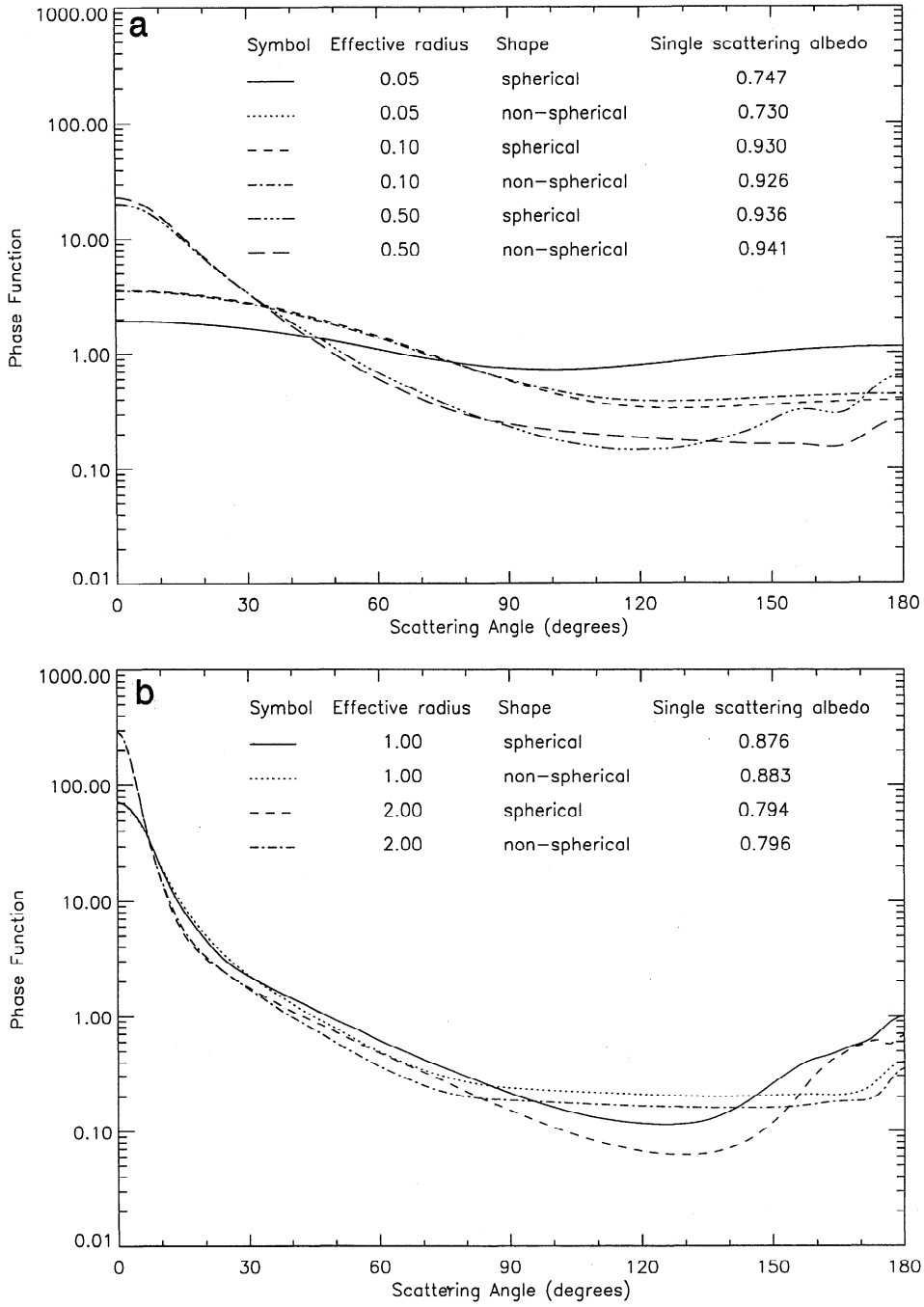


**Figure 1.** Single-scattering phase functions for several pairs of spherical and nonspherical particles with the same values of $r_{eff}$. For all cases, $v_{eff} = 0.2$, and $\lambda$ is 670 nm. (a) For $r_{eff} = 0.05$ $\mu$m (note that the nonspherical case is hidden by the spherical case for this size particle); $r_{eff} = 0.1$ $\mu$m, and $r_{eff} = 0.5$ $\mu$m; (b) $r_{eff} = 1.0$ $\mu$m, and $r_{eff} = 2.0$ $\mu$m.

a sphere with equal surface area for nonspherical particles. $C$ is a normalization constant for the distribution. The parameters $r_1$ and $r_2$ are selected so that the cross-section mean-weighted radius of the distribution as a whole is $r_{eff}$ and the variance of the distribution is $v_{eff}$ [*Mishchenko and Travis*, 1994]. For all cases, $v_{eff}$ is 0.2, and the particle index of refraction is $1.53 - 0.008i$, independent of wavelength. The wavelength dependence of single-scattering properties scales as $x$, where $x = 2 \pi r/\lambda$, and $\lambda$ is the wavelength [*Hansen and Travis*, 1974]. Unless specified otherwise, optical properties presented in this paper are for MISR band 3 (670 nm); in the underlying calculations, optical properties are properly scaled to account for wavelength dependence in each of the MISR bands used.

Figure 1 compares the single-scattering phase functions for distributions of spherical and nonspherical particles of several effective sizes. Only particles larger than the smallest ones shown in Figure 1 ($r_{eff} = 0.05$ $\mu$m) are thought to contribute significantly to the mineral dust optical depth of the atmosphere [e.g., *Tegen and Fung*, 1994]. The single-scattering

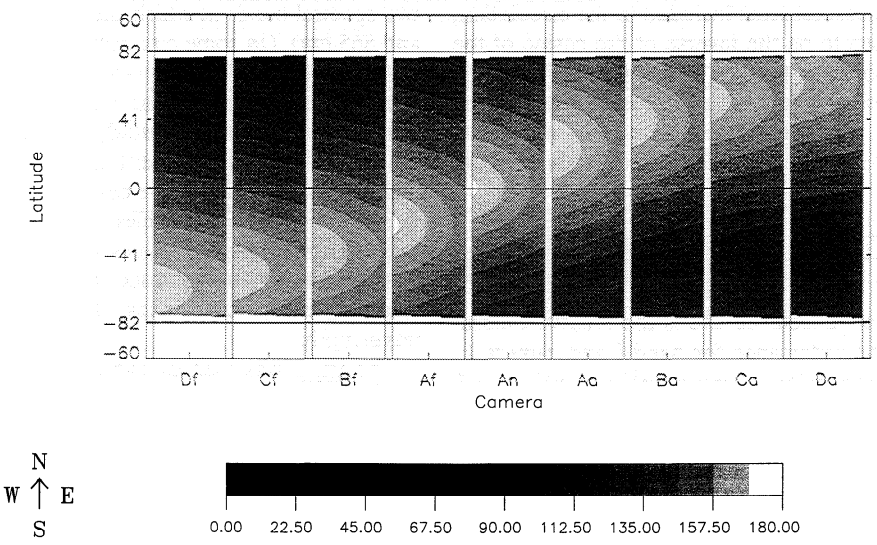


**Figure 2.** Range of scattering angles to be sampled by the nine multiangle imaging spectroradiometer (MISR) cameras, as functions of latitude and location in the instrument scan line, for March 21 and the nominal EOS-AM1 platform orbit. Each scan is 360 km wide. Sampling extends to 82° latitude and in some seasons folds over toward 60° in the opposing hemisphere. The pattern remains nearly the same but shifts poleward, as the solstice seasons approach.

phase functions for spherical and nonspherical particles at the smallest sizes are indistinguishable. Distributions with effective radii in the 0.5-to-10 $\mu$m range are typical of suspended atmospheric mineral dust aerosols [*Tegen and Fung*, 1994]. For these larger aerosols the nonspherical particles put a smaller fraction of the total scattering into the backscattering direction at scattering angles greater than about 150° and a larger fraction into the scattering angles between about 100° and 150°, compared to spherical particles with equivalent surface area. The characteristics shown in Figure 1 have been reproduced for other types of randomly oriented aggregates of nonspherical particles [e.g., *Takano and Liou*, 1989].

The optical properties given by *Mishchenko et al.* [1996] allow us to treat particles with sizes up to about 2 $\mu$m, which is adequate to cover the transition in single-scattering characteristics between particles with $x$ values in the small (Rayleigh) and large (geometric optics) regimes. Qualitatively, the results for the largest particles we can treat also apply to particles with effective radii between 2 and 10 $\mu$m. Quantitative treatment of the sensitivity of multiangle remote sensing to the larger particles requires additional calculations that are currently underway.

The scattering angle coverage for each of the 9 MISR cameras, as a function of latitude and location in the scan line, is shown in Figure 2 for March 21, for the nominal EOS-AM1 platform orbit. In midlatitudes, scattering angles between about 60° and 160° are covered by the nine cameras, whereas at high latitudes the range is approximately 40°–150° and at low latitudes, 100° to 160°. With changing seasons the pattern of coverage remains nearly the same but shifts toward the summer pole.

The MISR Team has developed a radiative transfer code, based on the adding-doubling method [*Hansen and Travis*, 1974], to simulate top-of-atmosphere reflectances as would be observed by the MISR instrument for arbitrary choice of aerosol type and amount and variable surface reflectance properties [*Diner et al.*, 1994]. For the present study we have simulated MISR measurements over a Fresnel-reflecting calm ocean surface, in a cloud-free, Rayleigh-scattering atmosphere with a surface pressure of 1.013 bar and a standard midlatitude temperature profile. A layer containing either nonspherical or spherical particles is placed between the gas component and the surface. (Sensitivity studies show that for the range of aerosol optical depth treated here, the results would be unaffected if the aerosols were modeled as mixed with the gas in the lowest part of the atmosphere.) The goal is to determine the degree to which we can distinguish between the nonspherical and spherical particle cases from the measurements.

As a measure of the sensitivity of the observations to aerosol properties, we use a normalized $\chi^2$ parameter that weights the contributions from each observed reflectance according to the slant path of the observation through the atmosphere. (In this paper, reflectance is defined as the radiance multiplied by $\pi$ and divided by the exoatmospheric solar irradiance at normal incidence.) The slant path weighting was chosen because measurements taken at steeper emission angles have greater sensitivity to the atmosphere in proportion to this factor. We use a $\chi^2$ statistic that includes the spectral dependence of the measurements but emphasizes the camera-to-camera geometric differences. We anticipate that such a parameter might provide good sensitivity to particle size as well as optical depth, given the MISR measurements. The simplest way to define this statistic is to divide each spectral measurement by the corresponding spectral measurement in the nadir camera:

$$\chi^2_{\text{geom}} = \frac{1}{N\langle m_k\rangle} \cdot \sum_{l=1}^{4} \sum_{\substack{k=1 \\ k\neq\text{nadir}}}^{9} \frac{m_k\left[\dfrac{L_{\text{meas}}(l,k)}{L_{\text{meas}}(l,\text{nadir})} - \dfrac{L_{\text{comp}}(l,k)}{L_{\text{comp}}(l,\text{nadir})}\right]^2}{\sigma^2_{\text{geom}}(l,k)} \quad (1)$$

where $L_{\text{meas}}$ is the simulated "measured" reflectance, $L_{\text{comp}}$ is the simulated reflectance for the "assumed" comparison model, $l$ and $k$ are the indices for wavelength band and camera,

$N$ is the number of measurements included in the calculation, $m_k$ are weights, chosen to be the inverse of the cosine of the emission angle appropriate to each camera $k$, $\langle m_k \rangle$ is the average of weights for all the measurements included in the calculation, and $\sigma_{\text{geom}}$ (a dimensionless quantity) is the uncertainty in the measured channel-to-channel reflectance ratio, given by

$$\sigma^2_{\text{geom}}(l, k) = \frac{\sigma^2_{\text{rel}}(l, k)}{L^2_{\text{meas}}(l, \text{nadir})} + \frac{L^2_{\text{meas}}(l, k)\sigma^2_{rel}(l, k)}{L^4_{\text{meas}}(l, \text{nadir})} \quad (2)$$

where $\sigma_{\text{rel}}$ has units of reflectance and is the relative calibration uncertainty in the reflectance for band $l$ and camera $k$. (Equation (2) is the expansion of errors: $\sigma^2[f(x, y)] = (df/dx)^2\,\sigma_x^2 + (df/dy)^2\,\sigma_y^2$ [e.g., *Bevington*, 1969]. In this case, $x$ is $L_{\text{meas}}(l, k)$ and $y$ is $L_{\text{meas}}(l, \text{nadir})$.) For the MISR instrument the value of $\sigma_{\text{rel}}$ is specified to fall between 0.01 for a target with reflectance of 100% and 0.02 for a reflectance of 5%, in all channels [*Diner et al.*, 1994]. For these simulations we model $\sigma_{\text{rel}}$ as varying linearly with reflectance. Note that $\sigma_{\text{rel}}$ includes the effects of systematic calibration errors for ratios of reflectance between channels. Random error due to instrument noise is negligible, based on the high signal-to-noise ratio demonstrated during MISR camera testing.

Since the $\chi^2$ parameter is normalized to the number of channels used, a value less than or about unity implies that the comparison model is indistinguishable from the measurements. Values larger than about 5 imply that the comparison model is not consistent with the observations. In more detail, $\chi^2 < 1$ means that the average difference between the measured and comparison quantities is less than the associated measurement error. The upper bound of 5 corresponds formally to an average confidence of better than 95% that we are not rejecting a comparison model when in fact it should be accepted.

To illustrate this in subsequent figures, we have developed a color bar with three segments: a logarithmic segment for values between $10^{-5}$ and 1 depicted in shades of blue, a logarithmic segment for values between 5 and $10^4$ depicted in shades of red, and a linear segment shown in light green, yellow, and orange shades for the intermediate values. Thus red shades in the figures indicate situations where the model is clearly distinguishable from the measurement, whereas blue shades indicate that the model is indistinguishable from the measurement. Black is reserved for exact agreement between model and measurement, which can occur in this study because we are working with simulated observations. Note that the color table has been designed so that if the color plates are photocopied in black and white, first-order information about the ability to distinguish among models is preserved.

## 3. Sensitivity of Multiangle, Multispectral Radiances to Particle Sphericity

In Plate 1a we address the question: If the atmosphere contains nonspherical particles with aerosol optical depth $\tau_{\text{a,atm}}$ and distribution of particles with effective radius $r_{\text{atm}}$, could a retrieval with MISR-like multispectral, multiangle data mistakenly interpret the measured reflectances as being due to spherical particles with effective radius $r_{\text{comp}}$ and aerosol optical depth $\tau_{a,\text{comp}}$?

For aerosol retrievals over ocean, the standard MISR algorithm uses data from all nine emission angles, but only in the two spectral bands at which the ocean surface is darkest (670 and 865 nm). (In some circumstances, sun glint will affect one or two of the MISR cameras. In the standard MISR aerosol retrievals, signals from these cameras will be excluded. For the purpose of this simulation study, we are interested in the greatest sensitivity the instrument can provide, so all cameras are included.) Simulations were performed for an atmosphere containing nonspherical particles with $r_{\text{atm}}$ values of 0.1, 0.5, 1.0, and 2.0 $\mu$m, and $\tau_{a,\text{atm}}$ values at 670 nm of 0.05, 0.2, and 0.8. Appropriate scaling was used to simulate the data at 865 nm, assuming the particle index of refraction is independent of wavelength.

The $\chi^2_{\text{geom}}$ was then calculated for comparison models that assume distributions of spherical particles with column optical depth $\tau_{a,\text{comp}}$ ranging from 0.05 to 1.0 in increments of 0.05, and effective radii $r_{\text{comp}}$ ranging from 0.1 to 2.0 $\mu$m, in increments of 0.1. According to Plate 1a, the $\chi^2_{\text{geom}}$ criterion is able to distinguish spherical from nonspherical particles for all cases chosen, except when the atmospheric particles are very small and $\tau_{a,\text{atm}}$ is low. We expect no discrimination for very small particles, since the corresponding spherical and nonspherical single-scattering phase functions are indistinguishable (Figure 1). Note that even for the very small particle case, the only value of $r_{\text{comp}}$ for which there is an acceptable match is the corresponding equivalent-sphere radius for $r_{\text{atm}}$, and the acceptable $\tau_{a,\text{comp}}$ values are within 0.05 of the corresponding value of $\tau_{a,\text{atm}}$.

Plate 1b tests the converse situation: nonspherical particles are assumed for the comparison models when the atmosphere actually contains spherical particles. Here again the only case where the difference in particle shape would not be detected is when the atmospheric particles are very small and $\tau_{a,\text{atm}}$ is low.

In addition, for very low atmospheric optical depth, some cases produce two local minima in $\chi^2_{\text{geom}}$ (though not low enough to qualify as acceptable matches). For the $r_{\text{atm}} = 0.5$ case, the minima occur when $r_{\text{comp}}$ is between 0.4 and 1.0 $\mu$m. These minima arise because the single-scattering albedo for the comparison (spherical) particles is slightly smaller than the corresponding value for nonspherical particles. As the comparison model optical depth is increased, the comparison model reflectance at the scattering angles measured by the instrument (60°–160°) also increases. For some intermediate value the difference in reflectance between the spherical and nonspherical cases reaches a local minimum. The absolute minimum and therefore the best fit optical depth still falls at the correct value. As comparison model optical depth increases further, the distinguishability becomes greater.

Similar results are obtained at poleward geometries. At low latitudes the range of scattering angle covered by MISR is diminished. Within about 20° of the subsolar latitude the scattering angle coverage only extends from 100° to 160° (Figure 2), limiting the sensitivity of the retrieval. This is particularly apparent for both the low optical depth and the small particle size cases, where the reflectance differences between spherical and nonspherical particles are small to begin with. For the smallest particle sizes tested the retrieval is insensitive to particle shape at low latitudes. For low optical depth the retrieval is insensitive to particle size and shape at these latitudes, but the retrieved optical depth is still within 0.05 of the correct value.

In Plate 2a we examine the ability of MISR-like measurements to correctly retrieve the properties of nonspherical particles. For this plate, both the atmosphere and comparison

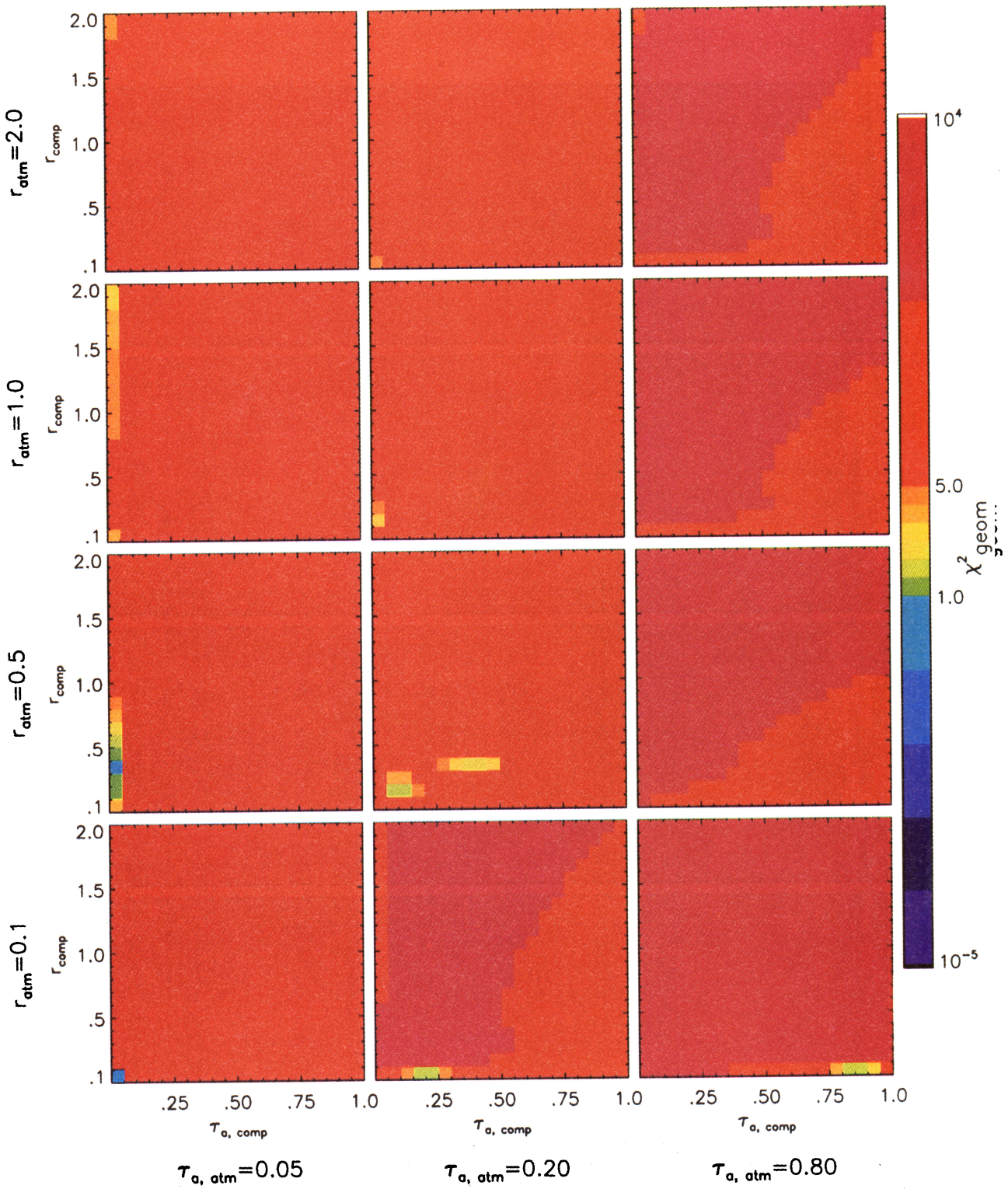


**Plate 1a.** Tests of the ability to distinguish spherical from nonspherical aerosols. For each panel, simulated MISR reflectances were produced for an atmosphere containing nonspherical particles with the specified $r_{atm}$ and $\tau_{a,atm}$. The $\tau_{a,atm}$ increases to the right from panel to panel, whereas $r_{atm}$ increases from panel to panel toward the top of the plate. The $\chi^2_{geom}$ was then calculated using the two longest wavelength MISR channels in all 9 cameras, for comparison models that assume distributions of spherical particles with effective radii $r_{comp}$ and column aerosol optical depth $\tau_{a,comp}$. All simulations presented are for midlatitude geometry over a Fresnel-reflecting, calm ocean surface, and include a standard Rayleigh scattering contribution. (In the plate, $\mu_0$ and $\Delta\phi_{Nadir}$ are the cosine of the solar incidence angle and the difference in azimuth between the Sun and nadir camera directions for the cases shown.) Colors indicating the value of $\chi^2_{geom}$ are plotted in each panel, with $r_{comp}$ increasing toward the top of each plot and $\tau_{a,comp}$ increasing to the right.

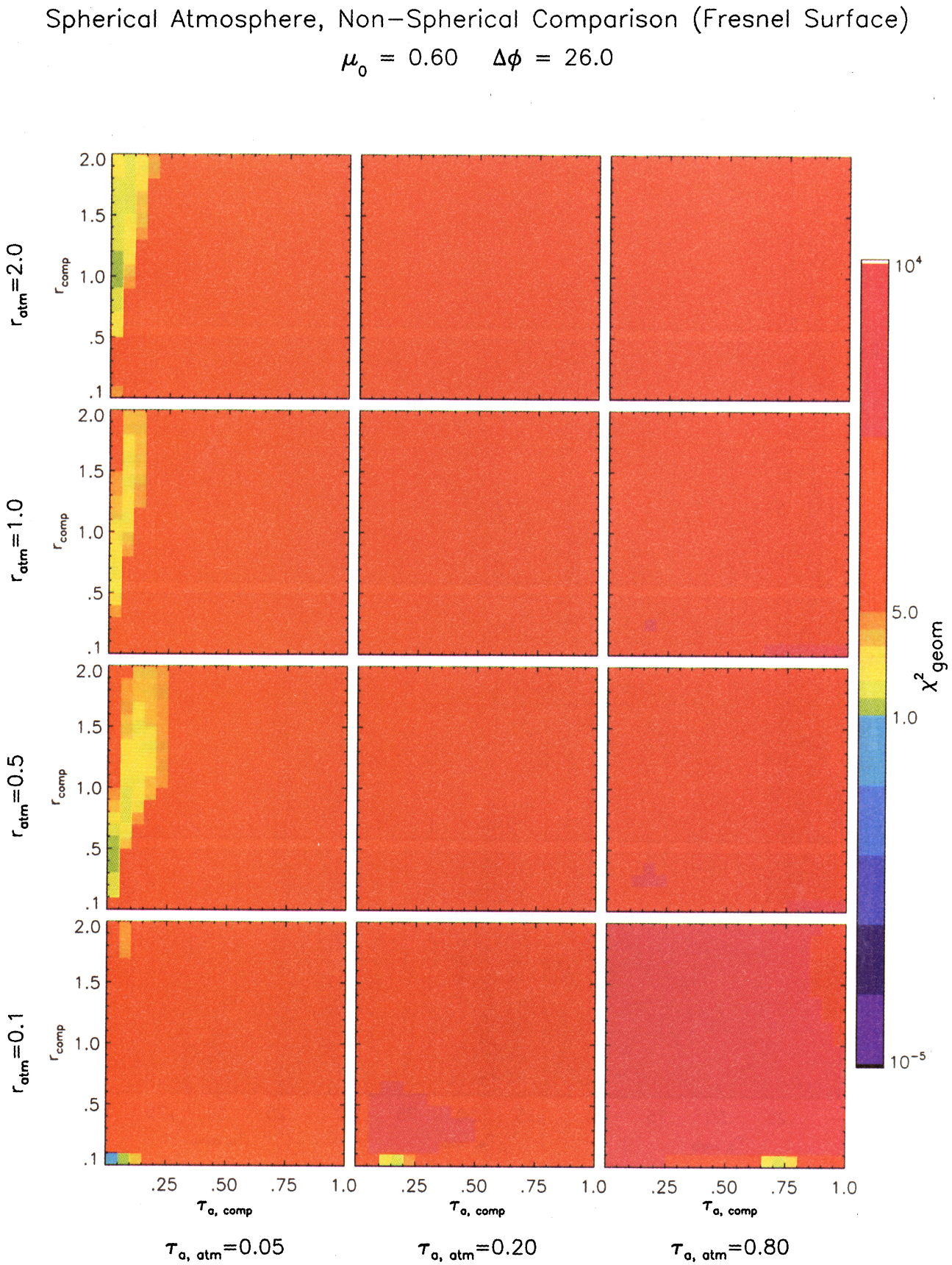


**Plate 1b.** Tests of the ability to distinguish spherical from nonspherical aerosols. Same as Plate 1a, except that the atmosphere is assumed to contain spherical particles, and comparison models assume nonspherical particles.

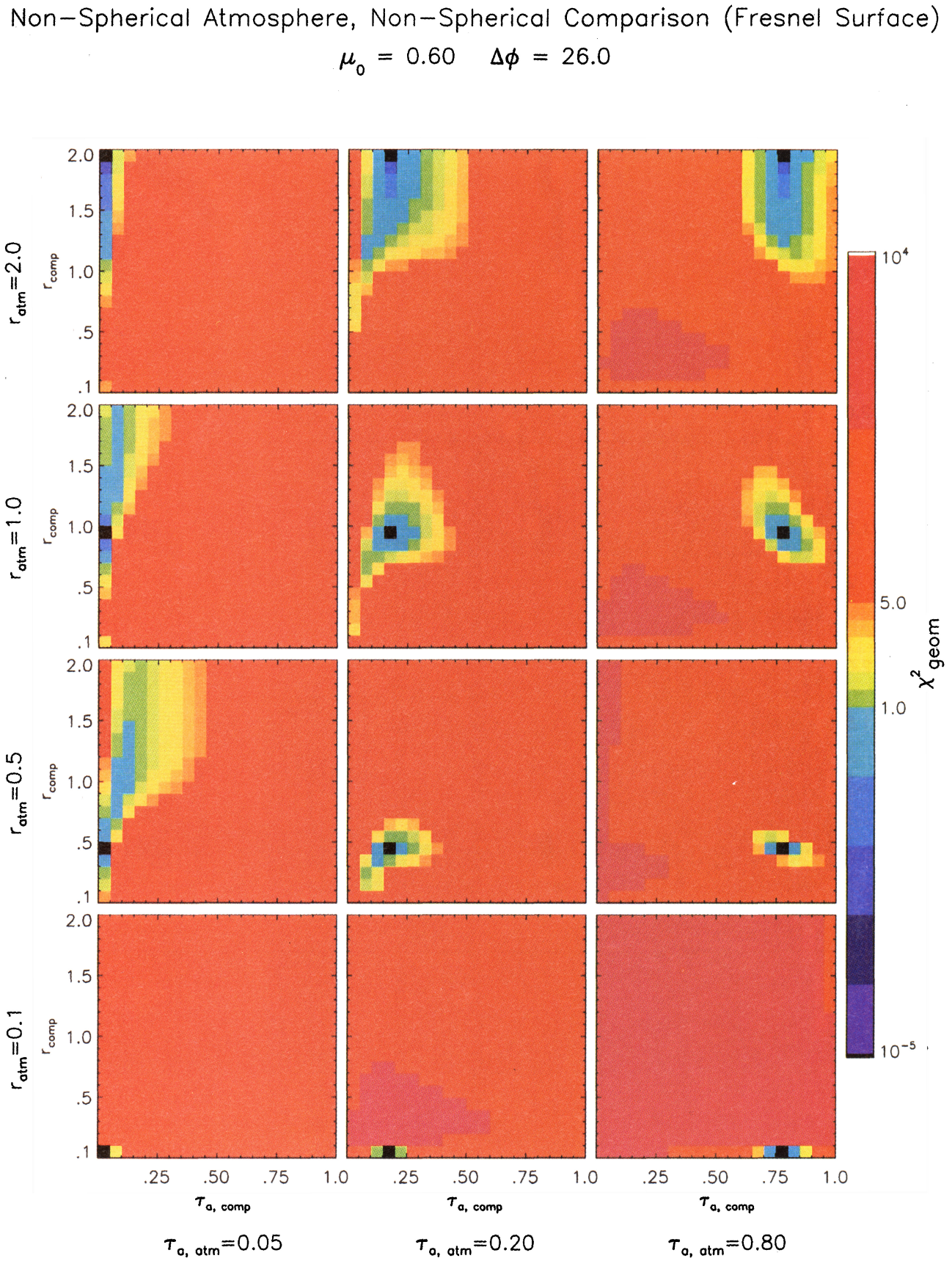


**Plate 2a.** Tests of the ability to constrain nonspherical aerosols. The $\chi^2_{geom}$ for the same parameter space as in Plate 1, except that the measured and comparison models both assume nonspherical particles.

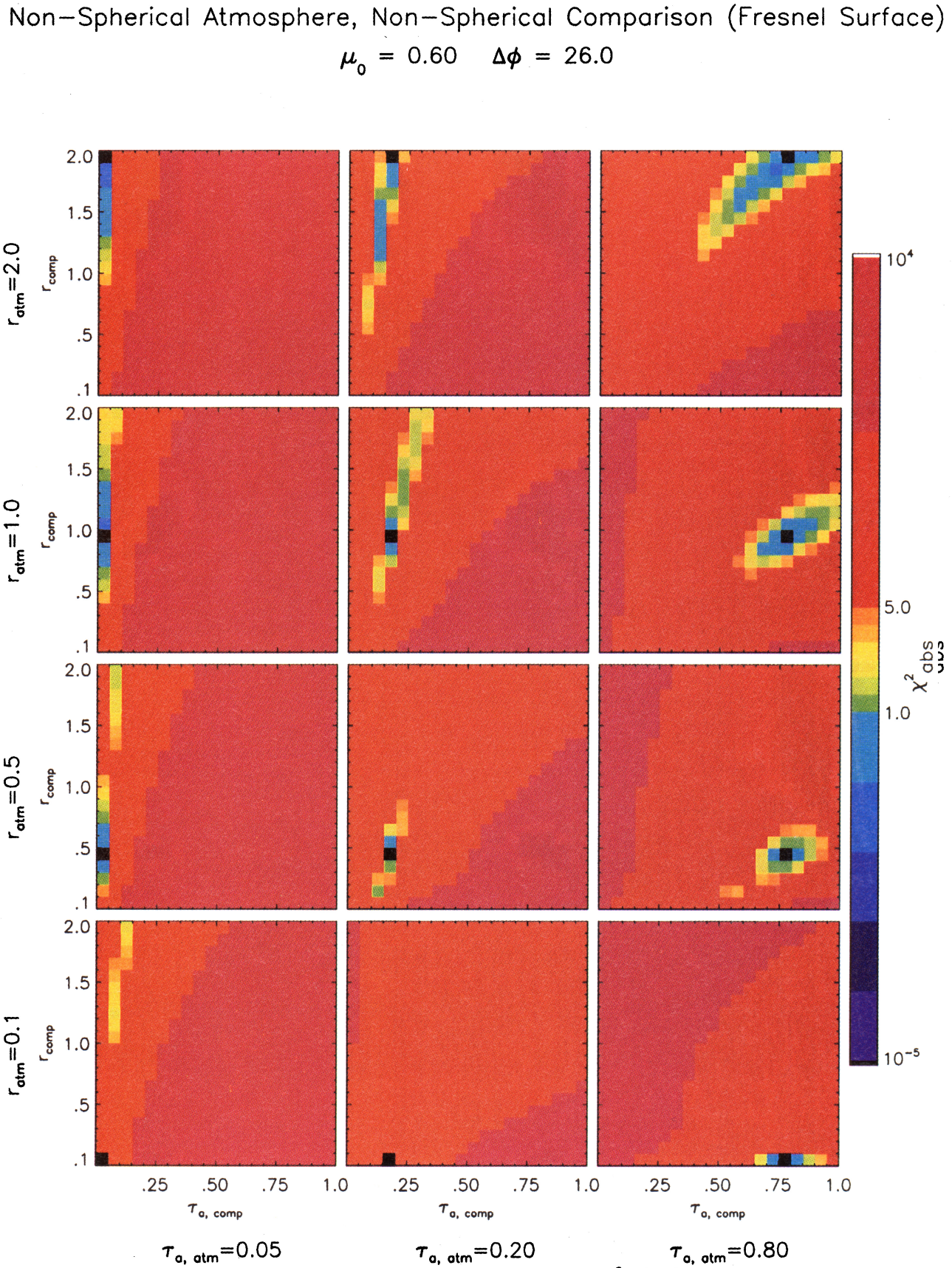


**Plate 2b.** Tests of the ability to constrain nonspherical aerosols. The $\chi^2_{abs}$ for the same parameter space as in Plate 2a.

models contain nonspherical particles. There are regions of acceptable matches for all cases, with exact agreement when the comparison model parameters equal those of the atmosphere. For low atmospheric optical depth and midsized to large sized atmospheric particles, a range of sizes satisfies the test. The size discrimination improves with increasing atmospheric optical depth, particularly for midsized particles.

The optical depth uncertainty is within 0.05 for small and 10% for larger particle sizes but is close to 50% for the worst case in Plate 2a. By using $\chi^2_{geom}$ alone, we have reduced 18 measurements to a single statistic. The $\chi^2_{geom}$ emphasizes the geometric properties of the scattering, which depend heavily on particle size and shape. However, there is more information in the measurements that may be used to improve the retrieval discrimination ability. For example, we define a statistic that weights the contributions from each observed absolute reflectance according to the slant path through the atmosphere of the observation:

$$\chi^2_{abs} = \frac{1}{N\langle m_k \rangle} \sum_{l=1}^{4} \sum_{k=1}^{9} \frac{m_k [L_{meas}(l, k) - L_{comp}(l, k)]^2}{\sigma^2_{abs}(l, k)} \quad (3)$$

where $\sigma_{abs}$ is the absolute measurement error in the reflectance; $\sigma_{abs}$ is nominally 3 times the corresponding value of $\sigma_{rel}$ for the MISR instrument [*Diner et al.*, 1994]. This statistic emphasizes the absolute reflectance, which depends heavily on optical depth. Plate 2b shows $\chi^2_{abs}$ for the same parameter space covered by $\chi^2_{geom}$ in Plate 2a. To fully use the additional information, a model must satisfy both $\chi^2$ criteria. This increases the retrieval sensitivity to optical depth to 10% or better over the entire parameter space. Combining the tests also improves slightly the retrieval sensitivity to particle size for larger particles. Size discrimination is poorest for low optical depth. Very similar results in terms of sensitivity to both optical depth and particle size are obtained at higher as well as lower latitudes.

## 4. Conclusions

Multiangle, multispectral measurements such as those anticipated from the EOS MISR instrument are sensitive to the characteristics of single-scattering phase functions that distinguish spherical from nonspherical particles. Simulated mixtures of nonspherical particles covering the range of size distributions and column abundances typical of atmospheric mineral dust over ocean were used, with indices of refraction representative of Sahara dust aerosol samples.

A simple $\chi^2$ test is adequate to distinguish spherical from nonspherical particles for indices of refraction typical of natural mineral dust, and for single-scattering phase functions characteristic of randomly oriented particles with a broad spectrum of sizes and shapes. The spherical-nonspherical distinction could not be made for the smallest particles tested, which have effective radii of 0.1 microns or less, and for low aerosol optical depths at latitudes within about 20° of the subsolar latitude. For the small particle cases the scattering properties themselves are indistinguishable from those of equivalent spheres, so the difference would have no effect on solar radiation balance calculations.

According to theoretical simulations, MISR-type measurements can retrieve column optical depth for nonspherical particles over calm ocean to an accuracy of at least 0.05 or 10%, whichever is larger. This is true even for cases where particle shape or size is not well-constrained by the retrieval. Two $\chi^2$ tests, one which emphasizes the geometric information in the measurement set, and one which emphasizes the absolute reflectances, are needed to produce these constraints. Constraints on effective radius vary with column optical depth and with the nature of the tests used for the retrieval. With the two $\chi^2$ tests adopted for this study, three to four distinct size groups between 0.1 and 2.0 microns effective radius are distinguishable over the assumed range of column optical depths.

Characterization of the sensitivity of MISR aerosol retrievals for a range of particle compositions and environmental conditions, and refinement of the criteria used for choosing "best fit" models, are part of continuing work. The MISR Team is currently performing sensitivity studies for aerosol column optical depth, aerosol size distribution, aerosol indices of refraction, aerosol hydration state, mixing of particle types, effects of thin cirrus, fogs, stratospheric aerosols, and underlying surface type.

**Acknowledgments.** We thank our colleagues D. Diner and J. Martonchik for many discussions of these topics. This research is performed at the Jet Propulsion Laboratory, California Institute of Technology, under contract with the National Aeronautics and Space Administration, and by the NASA Goddard Institute for Space Studies.

## References

Andreae, M. O., Climatic effects of changing atmospheric aerosol levels, in *World Survey of Climatology*, vol. 16, *Future Climates of the World*, edited by A. Henderson-Sellers, pp. 341–392, Elsevier, New York, 1995.

Bevington, P. R., *Data Reduction and Error Analysis for the Physical Sciences*, 366 pp., McGraw-Hill, New York, 1969.

Charlson, R. J., S. Schwartz, J. Hales, R. Cess, J. Coakley Jr., J. Hansen, and D. Hofmann, Climate forcing by anthropogenic aerosols, *Science*, *255*, 423–430, 1992.

Diner, D. J., C. J. Bruegge, J. V. Martonchik, G. W. Bothwell, E. D. Danielson, E. L. Floyd, V. G. Ford, L. E. Hovland, K. L. Jones, and M. L. White, A Multi-angle Imaging Spectroradiometer for terrestrial remote sensing from the Earth Observing System, *Int. J. Imaging Syst. Technol.*, *3*, 92–107, 1991.

Diner, J., W. Abdou, T. Ackerman, J. Conel, H. Gordon, R. Kahn, J. Martonchik, S. Paradise, M. Wang, and R. West, MISR level 2 algorithm theoretical basis: Aerosol/surface product, 1, Aerosol parameters, *Intern. Doc. D11400, Rev. A*, Jet Propul. Lab., Pasadena, Calif., 1994.

Hansen, J., and A. Lacis, Sun and dust versus greenhouse gases: An assessment of their relative roles in global climate change, *Nature*, *346*, 713–719, 1990.

Hansen, J. E., and L. D. Travis, Light scattering in planetary atmospheres, *Space Sci. Rev.*, *16*, 527–610, 1974.

Kiehl, J. T., and B. P. Briegleb, The relative roles of sulfate aerosols and greenhouse gases in climate forcing, *Science*, *260*, 311–314, 1993.

Mishchenko, M. I., and L. D. Travis, Light scattering by polydisperse, rotationally symmetric nonspherical particles: Linear polarization, *J. Quant. Spectrosc. Radiat. Transfer*, *51*, 759–778, 1994.

Mishchenko, M. I., A. A. Lacis, B. E. Carlson, and L. D. Travis, Nonsphericity of dust-like tropospheric aerosols: Implications for aerosol remote sensing and climate modeling, *Geophys. Res. Lett.*, *22*, 1077–1080, 1995.

Mishchenko, M. I., L. D. Travis, R. A. Kahn, and R. A. West, Modeling phase functions for dust-like tropospheric aerosols using a shape mixture of randomly oriented polydisperse spheroids, *J. Geophys. Res.*, this issue.

Penner, J. E., R. J. Charlson, J. M. Hales, N. S. Laulainen, R. Leifer, T. Novakov, J. Ogren, L. F. Radke, S. E. Schwartz, and L. Travis, Quantifying and minimizing uncertainty of climate forcing by anthropogenic aerosols, *Bull. Am. Meteorol. Soc.*, *75*, 375–400, 1994.

Rao, C. R. N., L. L. Stowe, and E. P. McClain, Remote sensing of aerosols over the oceans using AVHRR data: Theory, practice and applications, *Int. J. Remote Sens.*, *10*, 743–749, 1989.

Takano, Y., and K.-N. Liou, Solar radiative transfer in cirrus clouds, I, Single-scattering properties of hexagonal ice crystals, *J. Atmos. Sci.*, *46*, 3–19, 1989.

Tegen, I., and I. Fung, Modeling of mineral dust in the atmosphere: Sources, transport, and optical thickness, *J. Geophys. Res.*, *99*, 22,897–22,914, 1994.

West, R. A., L. R. Doose, A. M. Eibl, M. G. Tomasko, and M. I. Mishchenko, Laboratory measurements of mineral dust scattering phase function and linear polarization, *J. Geophys. Res.*, this issue.

R. Kahn, D. McDonald, B. Rheingans, and R. West, Jet Propulsion Laboratory, California Institute of Technology, 4800 Oak Grove Drive, Pasadena, CA 91109. (e-mail: kahn@jord.jpl.nasa.gov)

M. I. Mishchenko, NASA Goddard Institute for Space Studies, New York, NY 10025.

(Received January 10, 1996; revised May 30, 1996; accepted May 30, 1996.)